Optical Coherence Tomography Scan Circle Location and Mean Retinal Nerve Fiber Layer Measurement Variability

Michelle L. Gabriele,[1,2,3] *Hiroshi Ishikawa,*[1,2,3] *Gadi Wollstein,*[1] *Richard A. Bilonick,*[1] *Kelly A. Townsend,*[1] *Larry Kagemann,*[1,2] *Maciej Wojtkowski,*[4,5] *Vivek J. Srinivasan,*[4] *James G. Fujimoto,*[4] *Jay S. Duker,*[6] *and Joel S. Schuman*[1,2]

Purpose. To investigate the effect on optical coherence tomography (OCT) retinal nerve fiber layer (RNFL) thickness measurements of varying the standard 3.4-mm-diameter circle location.

Methods. The optic nerve head (ONH) region of 17 eyes of 17 healthy subjects was imaged with high-speed, ultrahigh-resolution OCT (hsUHR-OCT; 501 × 180 axial scans covering a 6 × 6-mm area; scan time, 3.84 seconds) for a comprehensive sampling. This method allows for systematic simulation of the variable circle placement effect. RNFL thickness was measured on this three-dimensional dataset by using a custom-designed software program. RNFL thickness was resampled along a 3.4-mm-diameter circle centered on the ONH, then along 3.4-mm circles shifted horizontally (*x*-shift), vertically (*y*-shift) and diagonally up to ±500 μm (at 100-μm intervals). Linear mixed-effects models were used to determine RNFL thickness as a function of the scan circle shift. A model for the distance between the two thickest measurements along the RNFL thickness circular profile (peak distance) was also calculated.

Results. RNFL thickness tended to decrease with both positive and negative *x*- and *y*-shifts. The range of shifts that caused a decrease greater than the variability inherent to the commercial device was greater in both nasal and temporal quadrants than in the superior and inferior ones. The model for peak distance demonstrated that as the scan moves nasally, the RNFL peak distance increases, and as the circle moves temporally, the distance decreases. Vertical shifts had a minimal effect on peak distance.

Conclusions. The location of the OCT scan circle affects RNFL thickness measurements. Accurate registration of OCT scans is essential for measurement reproducibility and longitudinal examination (ClinicalTrials.gov number, NCT00286637). (*Invest Ophthalmol Vis Sci.* 2008;49:2315–2321) DOI:10.1167/iovs.07-0873

Accurate assessment of the retinal nerve fiber layer (RNFL) is an important component in the diagnosis and management of glaucoma.[1–3] Several imaging technologies are currently available for RNFL assessment, including optical coherence tomography (OCT).[4–13] Automated segmentation of the RNFL has permitted the quantification of RNFL thickness in OCT images.[14] These measurements are reproducible[15–17] and correlate well with the level of visual function[10,12] and glaucomatous severity.[18,19] OCT is capable of differentiating between glaucomatous and healthy eyes[11,12] and monitoring glaucomatous progression longitudinally.[13]

The current clinical standard for obtaining RNFL thickness measurements in the commercially available OCT system using time-domain detection (StratusOCT; Carl Zeiss Meditec, Inc., Dublin, CA) is a circular scan centered on the optic nerve head (ONH) with a diameter of 3.4 mm. Overall mean and sectoral (clock-hour and quadrants) RNFL thickness measurements are obtained from these images. This 3.4-mm-diameter circumpapillary scan location has been shown to be the most reproducible compared with scan circles of different diameters.[14,20] RNFL thickness measurements at this location have also shown high intra- and intersession reproducibility in healthy[21] and glaucomatous eyes in the commercially available device.[17] However, one potential source of measurement variability is the manual placement of the scan circle by the device operator. This variability could be especially confounding in longitudinal assessment, where detection of small thickness changes is desired.

Recently, improvements in OCT technology have allowed high-speed, ultrahigh-resolution OCT (hsUHR-OCT), using spectral and Fourier domain detection to provide increased sensitivity and scanning speed, compared with conventional OCT with time domain detection.[22–26] These improvements permit high-density, raster scanning of retinal tissue, which

From the [1]UPMC Eye Center, Eye and Ear Institute, Ophthalmology and Visual Science Research Center, Department of Ophthalmology, University of Pittsburgh School of Medicine, Pittsburgh, Pennsylvania; the [2]Department of Bioengineering, University of Pittsburgh School of Engineering, Pittsburgh, Pennsylvania; the [4]Department of Electrical Engineering and Computer Science and Research Laboratory of Electronics, Massachusetts Institute of Technology, Cambridge, Massachusetts; the [5]Institute of Physics, Nicolaus Copernicus University, Torun, Poland; and the [6]New England Eye Center, Tufts-New England Medical Center, Tufts University School of Medicine, Boston, Massachusetts.

[3]Contributed equally to the work and therefore should be considered equivalent authors.

Presented at the annual meeting of the Association for Research in Vision and Ophthalmology, Fort Lauderdale, Florida, May 2007.

Supported in part by National Institutes of Health contracts R01-EY13178-08, R01-EY11289-22, and P30-EY08098-21 (Bethesda, MD), National Science Foundation contract BES-0522845 (Arlington, VA), Air Force Office of Scientific Research contract FA9550-040-1-0011 (Arlington, VA), Medical Free Electron Laser Program contract FA9550-040-1-0046 (Arlington, VA), The Eye and Ear Foundation (Pittsburgh, PA), and unrestricted grants from Research to Prevent Blindness, Inc. (New York, NY). JSS and JGF receive royalties for intellectual property licensed by Massachusetts Institute of Technology to Carl Zeiss Meditec.

Submitted for publication July 11, 2007; revised August 31 and November 21, 2007, and February 1, 2008; accepted April 14, 2008.

Disclosure: **M.L. Gabriele**, None; **H. Ishikawa**, None; **G. Wollstein**, Carl Zeiss Meditec, Inc. (F); **R.A. Bilonick**, None; **K.A. Townsend**, None; **L. Kagemann**, None; **M. Wojtkowski**, None; **V.J. Srinivasan**, None; **J.G. Fujimoto**, P; **J.S. Duker**, None; **J.S. Schuman**, P

The publication costs of this article were defrayed in part by page charge payment. This article must therefore be marked "*advertisement*" in accordance with 18 U.S.C. §1734 solely to indicate this fact.

Corresponding author: Gadi Wollstein, UPMC Eye Center, Department of Ophthalmology, University of Pittsburgh School of Medicine, 203 Lothrop Street, Eye and Ear Institute, Suite 834, Pittsburgh, PA 15213; wollsteing@upmc.edu.

enables three-dimensional reconstruction of the scanned area. It is then possible to detect and segment the RNFL in each raster OCT image, resample these data, and reconstruct arbitrary tissue-sampling patterns.

The goal of this study was to investigate the effect of the standard 3.4-mm-diameter circle location on RNFL thickness measurements. hsUHR-OCT raster images were used to obtain a homogenous sample of RNFL measurements. This method allowed for controlled shifting of the 3.4-mm circle with respect to the center of the ONH and did not require obtaining multiple scans, which would be susceptible to eye movement and signal quality variability.

Materials and Methods

Seventeen healthy volunteers from the University of Pittsburgh Medical Center (UPMC) Eye Center were enrolled in this prospective study, which was approved by the University of Pittsburgh human investigational review board (IRB) and adhered to the Declaration of Helsinki and Health Insurance Portability and Accountability Act (HIPAA). All subjects provided written informed consent to participate in the study.

Inclusion criteria were best corrected visual acuity of 20/40 or better, spherical equivalent refractive error between ±6.0 D, no media opacity precluding hsUHR-OCT retinal scanning, normal clinical ocular examination with no evidence of peripapillary atrophy, and reliable 24-2 standard Swedish interactive thresholding algorithm (SITA) perimetry within normal limits. A reliable SITA result was defined as less than 30% fixation losses and false-positive and -negative responses. Normal visual field was defined as glaucoma hemifield test (GHT) results within normal limits. If both eyes were eligible, one eye was randomly selected for the study.

Instrument

All subjects had hsUHR-OCT raster scanning (512 × 180 axial scans in a 6 × 6-mm area; scan time, 3.84 seconds) of the ONH region without dilating the pupil. A detailed description of this prototype hsUHR-OCT instrument has been published.[25] The device used in this study, however, had a multiplexed superluminescent diode light source (Broadlighter; Superlum Diodes, Moscow, Russia) with 100-nm bandwidth (full width at half maximum) and a center wavelength of 840 nm. This corresponded to an axial resolution of ~3.4 μm in tissue. The system had an A-scan acquisition rate of 24 kHz, resulting in an acquisition time of 3.84 seconds for each raster three-dimensional OCT data set. A hsUHR-OCT en face fundus image was created for each three-dimensional data set by summing all pixel intensity values along individual A-scans. The resultant sum along each A-scan was the intensity value used for the pixel corresponding to that A-scan's location within the 2-D en face hsUHR-OCT fundus image.

hsUHR-OCT fundus images were used for evaluation of eye motion during the scans, as well as defining disc margins. Multiple three-dimensional data sets centered on the ONH were acquired for each subject, and the best-quality image was subjectively chosen and used for subsequent analysis. Criteria for acceptable hsUHR-OCT fundus images included no large eye movements, which were defined as an abrupt shift in a large retinal vessel that completely disconnected the vessel in greater than three consecutive frames. In addition, we required that there be no signal dropouts (black bands in the fundus image caused by blinking during acquisition) and that there be consistent signal intensity level across the entire scan.

Image Analysis

The ONH margin for each subject was defined by one experienced operator (MG) by marking the edge of the ONH on the hsUHR-OCT fundus images with a series of points and spline interpolation. This method is analogous to that used to mark the disc margin in the commercially available confocal scanning laser ophthalmoscope. The geometric center of mass of this manually defined margin was then used to define the center of the optic disc for subsequent analysis.

We developed a custom software program to automatically segment the RNFL in each frame of the raster images by detecting the internal limiting membrane and outer RNFL border in each A-scan of each OCT frame.[27] RNFL thickness information along a 3.4-mm-diameter circle was resampled from the raster scan data, with the center of the circle corresponding to the geometric center of the optic disc. This 3.4-mm reconstructed circle represented the scan pattern that is currently used in the commercially available time-domain OCT system. The raster scan data were then resampled along this 3.4-mm-diameter circle shifted horizontally (*x*-shift), vertically (*y*-shift), and diagonally (45°–135°) up to ±500 μm (at 100-μm intervals between shift locations) with respect to the geometric center of the disc. Thus, 41 circles (one well-centered circle plus 10 circles shifted in four directions: horizontally, vertically, and along 45° and 135° diagonals) with a diameter of 3.4 mm were resampled for each subject. All data were normalized to the right eye to permit a comparison between quadrants from left and right eyes.

To ensure that a sufficient number of data points were sampled, individual shifted circles were excluded if there was a 0 thickness measurement along any given part of the circle. A 0 thickness could be recorded if a disc was off center during scanning and the resampled circle was outside of the scanning window, or if there was segmentation algorithm failure along the circle due to reduced signal level.

Statistical Analysis

Because each subject had repeated measurements, linear mixed-effects models were fitted to RNFL measurements (separately for the mean and the temporal, superior, nasal, inferior quadrants) and to peak distance, according to the approach outlined in Pinheiro and Bates[28] and using the R statistical programming language and environment (ver. 2.5.0 2007-04-23; http://www.R-project.org/R Development Core Team, 2007, R Foundation for Statistical Computing, Vienna, Austria). Peak distance was defined as the distance between the two thickest RNFL measurements along the RNFL thickness circular profile. This distance was automatically detected and measured with our custom software. In the statistical models for RNFL measurements and peak distance, random intercepts were included for subjects. Fixed effects were included for quadratic functions of the *x*- and *y*-shifts. A spatial correlation model was used to ensure that the parameter estimates, their standard errors, and their probabilities were well determined. Because our measurements were based on spatial information—RNFL thickness (or peak distance) depended on the degree of *x*- and *y*-shift from the center of the optic nerve—we could not assume that the experimental error would be statistically independent. A semivariogram analysis indicated that there was a strong dependency of the experimental errors as a function of the distance between *x*- and *y*-shift coordinates, and it was therefore necessary to find the most appropriate spatial correlation model to use in place of the statistical independence model. Likelihood ratio tests were used to assess the improvement due to the use of a spatial correlation error structure rather than the independence error model. The Akaike information criterion (AIC) was used to choose between competing models of spatial dependence. The spherical correlation model was optimal for all responses, with two exceptions. For nasal RNFL, a linear spatial correlation model was optimal. For peak distance, an exponential spatial correlation model was optimal. Confidence intervals were computed for all random effects, fixed effects, and spatial correlation parameters.

To provide a clinical context for our three-dimensional statistical models, we wanted to determine what magnitude of change is considered significant. We performed this determination by subtracting a threshold value from the maximum values of each of our models. Our thresholds were derived by scaling previously published expected error range measurements for the StratusOCT (mean RNFL thickness, 2.68 μm; temporal, 4.50 μm; superior, 4.39 μm; nasal, 8.20 μm; and inferior, 5.75 μm)[21] to our prototype device measurements (mean

TABLE 1. Linear Mixed-Effects Models for RNFL Thickness Parameters and Peak Distance, as a Function of the *x*- and *y*-Shifts

Mean RNFL = 148.43249 − 0.00788 · (*x*-shift) − 0.00003 · (*x*-shift)^2 + 0.00167 · (*y*-shift) − 0.00005 · (*y*-shift)^2
Temporal RNFL = 123.52417 − 0.00864 · (*x*-shift) − 0.00004 · (*x*-shift)^2 + 0.00332 · (*y*-shift) − 0.00001 · (*y*-shift)^2
Nasal RNFL = 131.40883 − 0.00842 · (*x*-shift) − 0.00004 · (*x*-shift)^2 + 0.01543 · (*y*-shift) − 0.00002 · (*y*-shift)^2
Superior RNFL = 168.80307 − 0.00939 · (*x*-shift) − 0.00003 · (*x*-shift)^2 + 0.01291 · (*y*-shift) − 0.00008 · (*y*-shift)^2
Inferior RNFL = 172.78499 − 0.00678 · (*x*-shift) − 0.00004 · (*x*-shift)^2 + 0.02392 · (*y*-shift) − 0.00011 · (*y*-shift)^2
Peak Distance = 5802.870 + 2.735 · (*x*-shift) − 0.002 · (*x*-shift)^2 + 0.267 · (*y*-shift)

Thickness parameters and peak distance are in micrometers.

RNFL thickness, 3.98 μm; temporal, 7.88 μm; superior, 5.97 μm; nasal, 13.60 μm; and inferior, 7.78 μm). The conversion between StratusOCT and prototype OCT measurements was accomplished using previously published RNFL thickness measurements.[29] Thus, a range of *y*-shifts (superior–inferior displacement of the center of the 3.4-mm circle from the center of the ONH) versus *x*-shifts (temporal–nasal displacement) corresponding to our thresholds was plotted. This plot then represented a maximum range of displacements when considering the effect of shift on thickness measurements. A displacement of the scanning circle (with respect to the center of the ONH) that is larger than the cutoffs may markedly change RNFL thickness and should be interpreted with caution.

RESULTS

Seventeen subjects were enrolled in the study (mean age, 39.6 ± 7.8 years; nine women, eight men, 11 right eyes and 6 left eyes). Fifteen (2.2%) of 697 3.4-mm circles were excluded from analysis because of a 0 μm thickness measurement along part of the circle (sampling outside of the scanning area). Twenty-six (3.7%) peak distance measurements were excluded because of algorithm failure. The linear mixed-effects models for mean and sectoral RNFL thicknesses and peak distance are shown in Table 1. A plot of mean RNFL thicknesses as a function of the *x*- and *y*-shift is shown in Figure 1. A plane marking the location where 3.98 μm (mean RNFL threshold level) was subtracted from the maximum value is also shown in this figure.

The effect of horizontal and vertical circle displacements on RNFL thickness and peak distance profiles is summarized in Figure 2. The model for peak distance was plotted over a shift range of ±500 μm in two graphs: *y*-shift equal to 0 (indicating horizontal shifts) and *x*-shift equal to 0 (vertical shifts; Fig. 3). A positive *x*-shift (nasal shift, Fig. 3a) caused an increase in the distance between peaks, and a negative *x*-shift (temporal shift) caused the peaks to move closer together. Vertical displacement of the circle had a minimal effect on the peak distance (Fig. 3b). It should be noted that, in vertical displacements, the peak distance remains relatively stable, but superior and inferior RNFL thicknesses change. Diagonal shifts are a combination of these horizontal and vertical displacements, with changes in both peak distance and quadrant thicknesses.

Figure 4 shows a range of *y*-shifts (vertical displacement of the center of the 3.4-mm circle from the center of the ONH) versus *x*-shifts (horizontal displacement) that correspond to our thresholds. This figure indicates the maximum range of displacements when considering shift effect on mean RNFL thickness (solid line) and was generated from the intersection of the plane and model shown in Figure 1. Also plotted in Figure 4 is the maximum range of *x*- and *y*-shifts when considering shift effect on sectoral (mean, temporal, superior, and inferior) RNFL thickness (dashed lines). Each ellipse in the graph therefore represents the limits of the location of the center of the 3.4-mm circle, with our threshold levels. For example, an *x*- and *y*-shift of 0 μm represents a well-centered scan circle: It is located within all ellipses and is thus an acceptable deviation. An *x*-shift of 100 μm and corresponding a *y*-shift of −100 μm represents an inferonasal shift. However, this inferonasal shift is within the ellipse and thus within the range of displacements that will not markedly affect mean

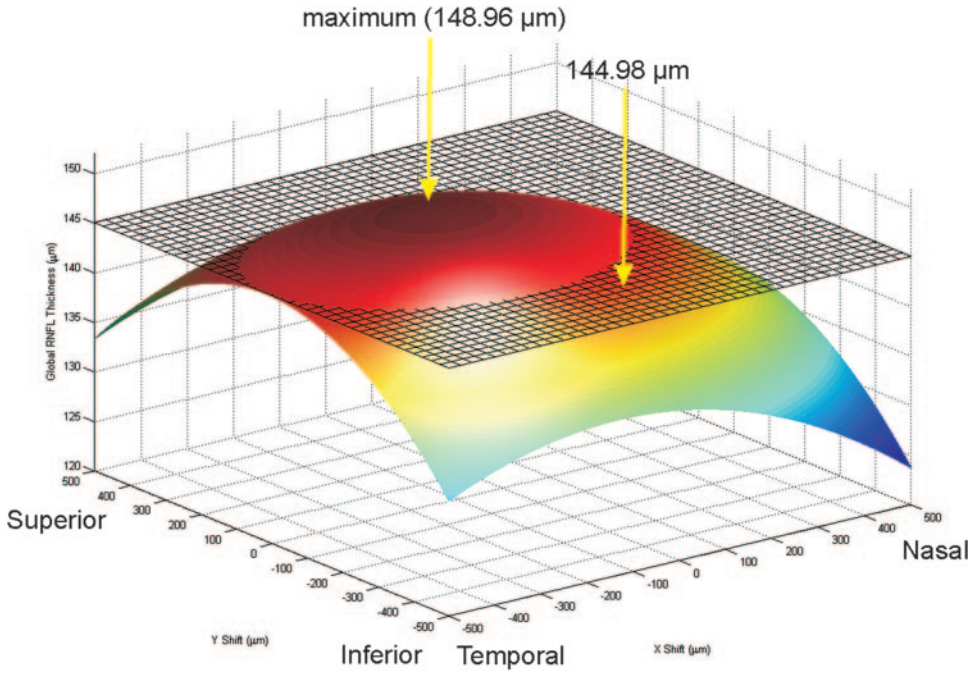

FIGURE 1. Plot of the linear mixed-effects model for mean RNFL thickness versus *x*- and *y*-shift. A plane transecting the model at a distance 3.98 μm from the maximum indicates our threshold level for mean RNFL thickness.

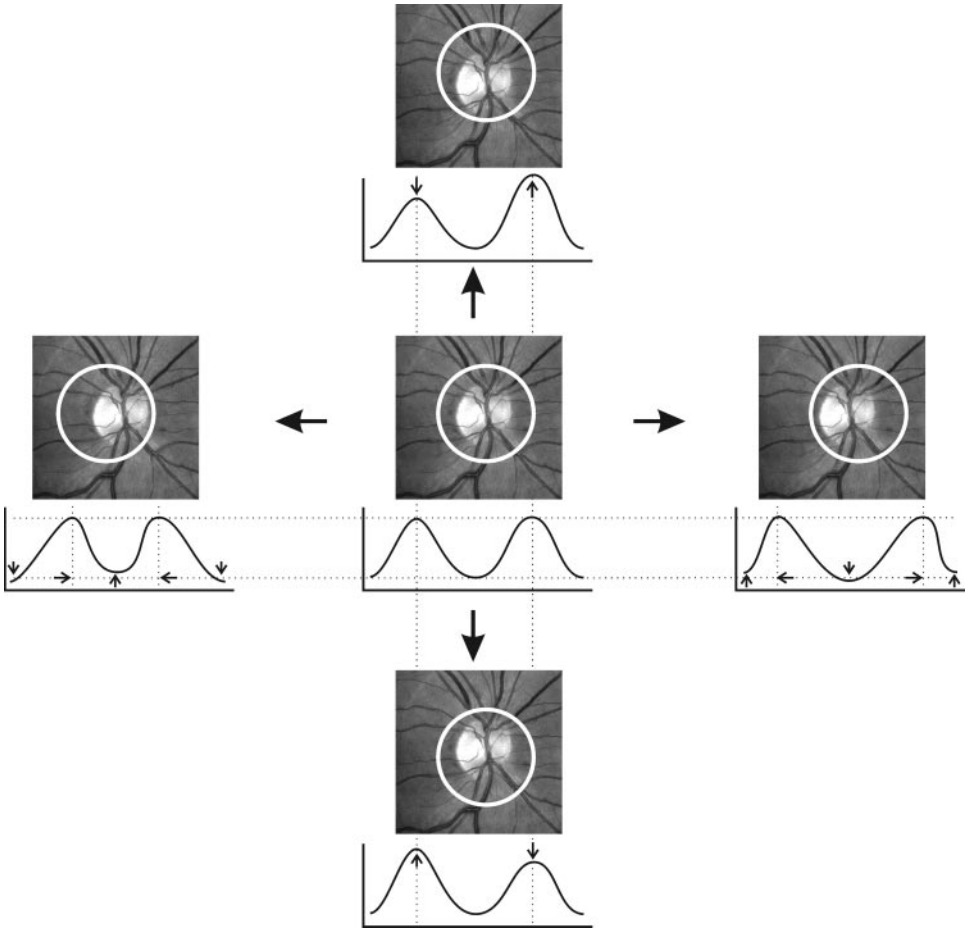

FIGURE 2. A summary of changes associated with horizontal and vertical scan circle displacements. When the scan circle was displaced horizontally, peak distance changes, but superior and inferior RNFL thicknesses remained stable. During vertical displacements, peak distance remained relatively stable, but the superior and inferior RNFL thicknesses changed.

RNFL. This shift is also within the limits for all sectoral cutoffs, although it is close to the cutoff for the inferior and superior quadrants. An *x*-shift of 200 μm and a *y*-shift of 600 μm (superonasal displacement), however, would be outside the maximum range of displacement when considering the effect of shift on mean, inferior quadrant, and superior quadrant RNFL thicknesses but within the cutoff for the temporal and nasal quadrants. Both nasal and temporal ranges of displacement in the *y*-shift direction were higher than the ranges for mean, superior and inferior RNFL thickness. Thus, even large displacements from the center of the ONH had a minimal effect on temporal and nasal RNFL measurements. The ranges of displacements when considering the shift effect on mean, superior, and inferior RNFL thicknesses were larger in the horizontal than the vertical direction, and thus mean, superior, and inferior RNFL thicknesses were affected more by vertical shifts than horizontal. The range of displacements for temporal RNFL measurements showed a similar configuration, rotated by 90°. The ellipse representing the range of displacements that affect mean RNFL measurements (Fig. 4) was scaled and super-

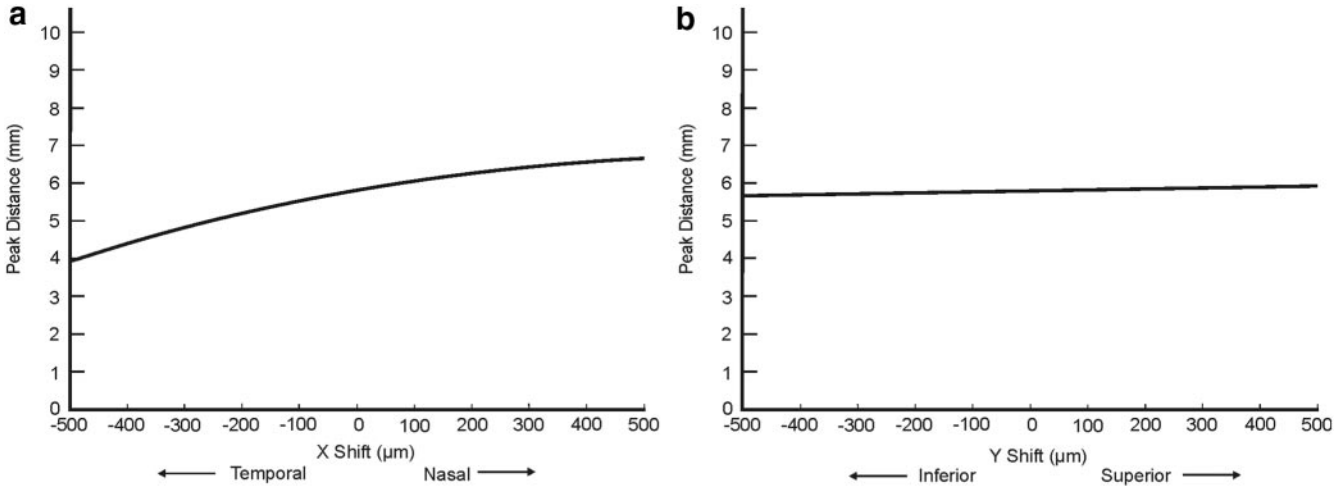

FIGURE 3. Plot of the peak distance as a function of *x*-shift with *y*-shift set to 0 (**a**), and *y*-shift with *x*-shift set to 0 (**b**).

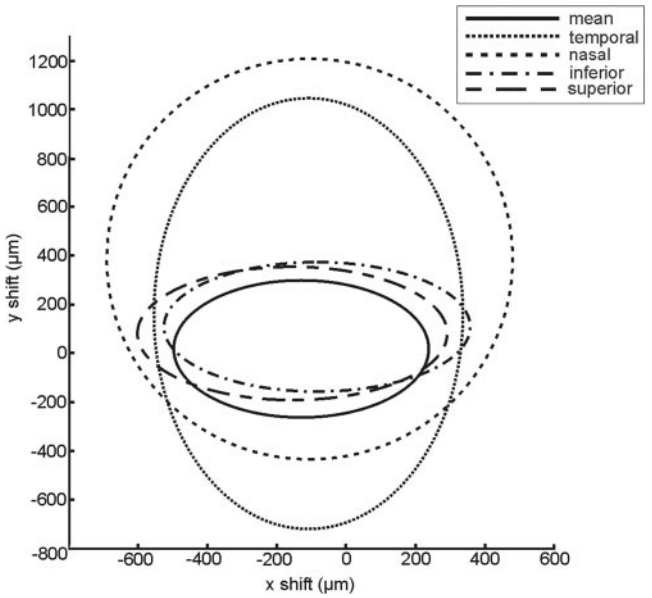

FIGURE 4. A plot of the maximum range of displacement of the center of the 3.4-mm scan circle for the mean and the quadrants, derived from the linear mixed-effects models and thresholds. The *x*-shifts (horizontal displacements of the center of the 3.4-mm circle from the center of the ONH) and *y*-shifts (vertical displacements) outside of these ellipses should be interpreted with caution.

imposed onto a hsUHR-OCT en face image, to demonstrate the magnitude of this effect (Fig. 5).

DISCUSSION

Our results demonstrate that scan circle location may add substantial variability to OCT measurements. It is interesting to note that regional RNFL thickness measurements were affected in different ways by scan displacement. For example, the maximum range of displacements when considering shift effect on mean RNFL and superior and inferior quadrant RNFL thicknesses showed a horizontally elongated elliptical shape, whereas the temporal quadrant showed a vertically elongated ellipse and the nasal quadrant showed a near-perfect circle (Fig. 4). The area within a given ellipse is dependent on our preset threshold levels: The nasal segment had the largest threshold and thus had the largest elliptical area.

Understanding the three-dimensional structural distribution of the RNFL, however, may help explain the horizontally and vertically elongated ellipses.[29] Histomorphologic and imaging studies have shown that the maximum RNFL thickness appears in the superotemporal and inferotemporal regions.[14,30,31] Any shift in the location of the scan circle that brings a sector closer to the disc margin causes a thickness increase in this region and a decrease in the opposite region. Any shift that brings the thickened RNFL bundles into the sector will also induce an increase in thickness. A downward displacement of the circle brings the scan circle closer to the disc margin in the superior quadrant, with subsequent thickening of RNFL measurements in that quadrant and thinning in the inferior quadrant. A nasal displacement of the scan brings the thickened bundles of the RNFL into the temporal region and causes an increased thickness in that region. As the superotemporal and inferotemporal bundles do not transect the nasal quadrant, changes in thickness in this region are only related to the proximity to the disc margin and thus result in the near-perfect circular pattern in Figure 4.

The horizontally elongated ellipses representing the maximum range of displacements for the mean and the superior and inferior quadrants signified that a small vertical displacement of the circle had a substantially larger effect on RNFL measurements than did a horizontal shift (Fig. 4). In the temporal quadrant, horizontal shifts had a larger effect than did vertical shifts, as reflected by the ellipse elongated in the vertical direction. All the ellipses were shifted superotemporally, perhaps due to a tendency of the operator when defining all the disc margins.

Our results show that the distance between the two humps in the RNFL profile changes as the scan circle is displaced horizontally (Fig. 3). A vertical displacement did not affect the peak distance but altered the height of each peak (Fig. 2).

The results of this study should be taken into account when comparing consecutive OCT scans, as they may explain some of the variability observed between scans. This variability affects cross-sectional glaucoma detection as well as longitudinal glaucoma progression assessment. A clinical example showing how circle displacement can affect the classification of quadrant measurements is provided in Figure 6. On the basis of our results, we hypothesize that it may be possible to predict the amount of change in RNFL measurements that correspond to a given shift amount, which would then allow an adjustment of measurements that are not well centered. Future studies to test this hypothesis are warranted.

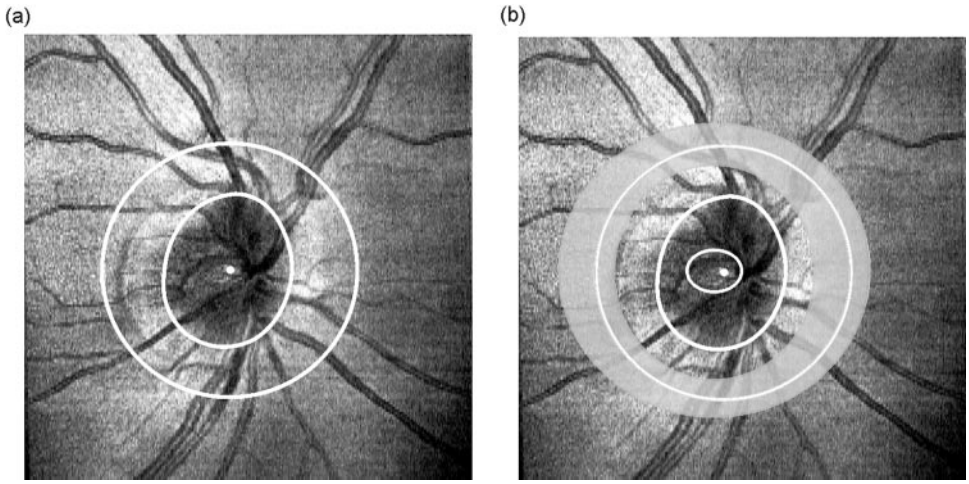

FIGURE 5. (**a**) High-speed, ultrahigh-resolution OCT fundus image with the disc margin manually drawn, the geometric center of the disc (*single white dot*), and a 3.4-mm circle centered on the disc. (**b**) *Inner ring*: range of possible locations of the center of the circle; *shaded area*: the corresponding locations of the 3.4-mm circle that will not affect mean RNFL thickness measurements beyond the threshold level (3.98 μm).

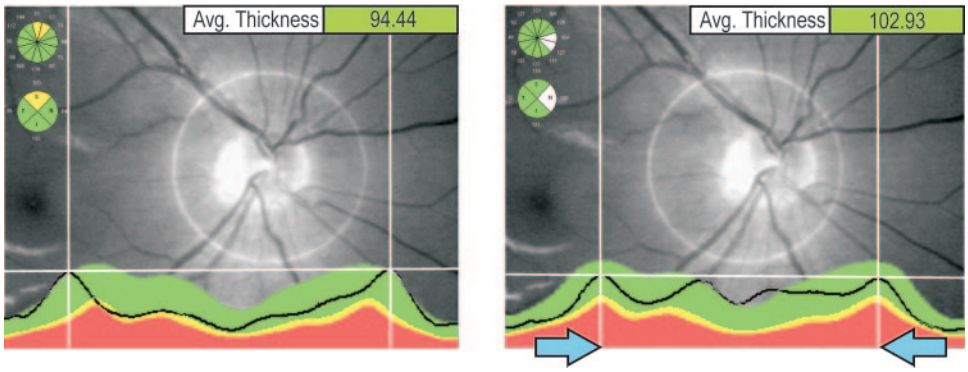

FIGURE 6. An example of a Stratus-OCT scan showing circle placement errors and corresponding changes in peak distance. *Left*: A well-centered scan. *Right*: As the scan circle is displaced temporally, the peaks move closer together and superior quadrant and clock hours measurements change from borderline (*yellow*) to normal (*green*) while nasal quadrants and clock hours become thicker.

One of the limitations of this study is that the circle shift amount was limited to ±500 μm, whereas our threshold limits were more than 600 μm in some cases. The results are extrapolated based on the assumption that the data outside of the shifting range fit the same quadratic model. We restricted the range to ±500 μm to ensure that most of the resampled circles were within the 6 × 6-mm scanning window, regardless of the small disc center offset within the scanning window. Further investigation is needed to clarify the effect of a shift beyond 500 μm.

Another limitation is that the prototype hsUHR-OCT device used in this study had a relatively long scanning duration (3.84 seconds) and uneven sampling density in *x*- and *y*-shift directions (512 × 180 sampling points). We excluded images with obvious eye motion, but there may have been small, undetected eye movements within the scans. We chose to use our prototype device in this study because its unique properties outweigh the limitations. The device that we used has better axial resolution than any commercially available OCT device, which gave us greater accuracy in our measurements. Further, none of the commercial spectral-domain OCT devices have been validated, nor do they have software capable of facilitating a study such as this. We created our own software to access these detailed data. However, because our findings are based on the ocular structure of the peripapillary region, our results can be generalized to any type of OCT circumpapillary scan.

The method presented in this article for resampling the 3.4-mm diameter circle after defining the disc margin and disc center may provide a way to have consistent sampling as patients are observed longitudinally by hsUHR-OCT. Although hsUHR-OCT does not eliminate eye motion, this method would lead to more precise registration from image to image, provided there was little eye motion or a method of correcting eye motion. This resampling method could be used with other scan patterns in addition to raster scanning. If a method for marking the disc margin could be developed for the StratusOCT, the disc center could be calculated and used to improve registration. One way to accomplish this would be to mark the disc margin on the live fundus image. With the current iteration of StratusOCT, however, the exact location of the scan circle cannot be determined.

In conclusion, the location of the OCT scan circle affects RNFL thickness measurements. Accurate registration of OCT scans is therefore important for measurement reproducibility and longitudinal examination and should be taken into account when comparing scans over time.

References

1. Hoyt WH, Frisen L, Newman NM. Fundoscopy of nerve fiber layer defects in glaucoma. *Invest Ophthalmol Vis Sci*. 1973;12:814–829.
2. Quigley HA, Miller NR, George T. Clinical evaluation of nerve fiber layer atrophy as an indicator of glaucomatous optic nerve damage. *Arch Ophthalmol*. 1980;98(9):1564–1571.
3. Airaksinen PJ, Drance SM, Douglas GR, et al. Diffuse and localized nerve fiber loss in glaucoma. *Am J Ophthalmol*. 1984;98:566–71.
4. Huang D, Swanson EA, Lin CP, et al. Optical coherence tomography. *Science*. 119:254;1178–1181.
5. Hee MR, Izatt, JA, Swanson EA, et al. Optical coherence tomography of the human retina. *Arch Ophthalmol*. 1995;113(3):325–332.
6. Mainster MA, Timberlake GT, Webb RH, Hughes GW. Scanning laser ophthalmoscopy: clinical applications. *Ophthalmology*. 1982;89(7):852–857.
7. Weinreb RN, Shakiba S, Zangwill L. Scanning laser polarimetry to measure the nerve fiber layer of normal and glaucomatous eyes. *Am J Ophthalmol*. 1995;119(5):627–636.
8. Pieroth L, Schuman JS, Hertzmark E, et al. Evaluation of focal defects of the nerve fiber layer using optical coherence tomography. *Ophthalmology*. 1999;106(3):570–579.
9. Jeoung JW, Park KH, Kim TW, et al. Diagnostic ability of optical coherence tomography with a normative database to detect localized retinal nerve fiber layer defects. *Ophthalmology*. 2005; 112(12):2157–2163.
10. El Beltagi TA, Bowd C, Boden C, et al. Retinal nerve fiber layer thickness measured with optical coherence tomography is related to visual function in glaucomatous eyes. *Ophthalmology*. 2003; 110(11):2185–2191.
11. Mistlberger A, Liebmann JM, Greenfield DS, et al. Heidelberg retina tomography and optical coherence tomography in normal, ocular-hypertensive, and glaucomatous eyes. *Ophthalmology*. 1999; 106(10):2027–2032.
12. Hoh ST, Greenfield DS, Mistlberger A, et al. Optical coherence tomography and scanning laser polarimetry in normal, ocular hypertensive, and glaucomatous eyes. *Am J Ophthalmol*. 2000; 129(2):129–135.
13. Wollstein G, Schuman JS, Price LL, et al. Optical coherence tomography longitudinal evaluation of retinal nerve fiber layer thickness in glaucoma. *Arch Ophthalmol*. 2005;123(4):464–470.
14. Schuman JS, Hee MR, Puliafito CA, et al. Quantification of nerve fiber layer thickness in normal and glaucomatous eyes using optical coherence tomography. *Arch Ophthalmol*. 1995;113(5):586–596.
15. Schuman JS, Pedut-Kloizman T, Hertzmark E, et al. Reproducibility of nerve fiber layer thickness measurements using optical coherence tomography. *Ophthalmology*. 1996;103(11):1889–1898.
16. Blumenthal EZ, Williams JM, Weinreb RN, et al. Reproducibility of nerve fiber layer thickness measurements by use of optical coherence tomography. *Ophthalmology*. 2000;107(12):2278–2282.
17. Budenz DL, Chang RT, Huang X, et al. Reproducibility of retinal nerve fiber thickness measurements using the stratus OCT in normal and glaucomatous eyes. *Invest Ophthalmol Vis Sci*. 2005; 46(7):2440–2443.
18. Guedes V, Schuman JS, Hertzmark E, et al. Optical coherence tomography measurement of macular and nerve fiber layer thickness in normal and glaucomatous human eyes. *Ophthalmology*. 2003;110(1):177–189.

19. Sihota R, Sony P, Gupta V, et al. Diagnostic capability of optical coherence tomography in evaluating the degree of glaucomatous retinal nerve fiber damage. *Invest Ophthalmol Vis Sci*. 2006;47(5): 2006–2010.
20. Carpineto P, Ciancaglini M, Zuppardi E, et al. Reliability of nerve fiber layer thickness measurements using optical coherence tomography in normal and glaucomatous eyes. *Ophthalmology*. 2003;110(1):190–195.
21. Paunescu LA, Schuman JS, Price LL, et al. Reproducibility of nerve fiber thickness, macular thickness, and optic nerve head measurements using StratusOCT. *Invest Ophthalmol Vis Sci*. 2004;45(6): 1716–1724.
22. Leitgeb RA, Hitzenberger CK, Fercher AF. Performance of Fourier domain vs. time domain optical coherence tomography. *Opt Express*. 2003;11(8):889–894.
23. de Boer JF, Cense B, Park BH, et al. Improved signal-to-noise ratio in spectral-domain compared with time-domain optical coherence tomography. *Opt Lett*. 2003;28(21):2067–2069.
24. Choma MA, Sarunic MV, Yang C, Izatt JA. Sensitivity advantage of swept source and Fourier domain optical coherence tomography. *Opt Express*. 2003;11(18):2183–2189.
25. Wojtkowski M, Srinivasan VJ, Ko TH, et al. Ultrahigh-resolution, high-speed, Fourier domain optical coherence tomography and methods for dispersion compensation. *Opt Express*. 2004; 12(11)2404–2422.
26. Nassif N, Cense B, Park BH, et al. In vivo human retinal imaging by ultrahigh-speed spectral domain optical coherence tomography. *Opt Lett*. 2004;1:29(5):480–482.
27. Ishikawa H, Piette S, Liebmann JM, Ritch R. Detecting the inner and outer borders of the retinal nerve fiber layer using optical coherence tomography. *Graefes Arch Clin Exp Ophthalmol*. 2002; 240(5):362–371.
28. Pinheiro JC, Bates DM. *Mixed-Effects Models in S and S-Plus*. New York: Springer Verlag; 2000.
29. Gabriele ML, Ishikawa H, Wollstein G, et al. Peripapillary nerve fiber layer thickness profile determined with high speed, ultrahigh resolution optical coherence tomography high-density scanning. *Invest Ophthalmol Vis Sci*. 2007;48(7):3154–3160.
30. Varma R, Skaf M, Barron E. Retinal nerve fiber layer thickness in normal human eyes. *Ophthalmology*. 1996;103(12):2114–2119.
31. Radius RL, Anderson DR. The course of axons through the retina and optic nerve head. *Arch Ophthalmol*. 1979;97(6)1154–1158.